Nanoelectronics and Its New Materials –
A NEW ERA OF NANOSCIENCE

Nanoelectronics and Its New Materials –
A NEW ERA OF NANOSCIENCE

ZEISS
Seeing beyond

WILEY

Discover the recent advances in electronics research and fundamental nanoscience.

Nanotechnology has become the driving force behind breakthroughs in engineering, materials science, physics, chemistry, and biological sciences. In this compendium, we delve into a wide range of novel applications that highlight recent advances in electronics research and fundamental nanoscience. From surface analysis and defect detection to tailored optical functionality and transparent nanowire electrodes, this eBook covers key topics that will revolutionize the future of electronics.

To get your hands on this valuable resource and unleash the power of nanotechnology, simply download the eBook now. Stay ahead of the curve and embrace the future of electronics with nanoscience as your guide.

ZEISS
Seeing beyond

WILEY

Bidirectional and Dual-Mode Organic Photodetector Enables Secure Ultraviolet Communication

Tingting Yan, Ziqing Li, Li Su, Limin Wu,* and Xiaosheng Fang*

Traditional optical communication mode with single-band photodetector depicts terrible confidentiality and it depends on sophisticated cryptography schemes to obtain a secure communication process. Dual-band photodetectors have potential to realize a secure optical communication with a straightforward optical encryption strategy. However, previous reports of dual-band organic photodetectors (OPD) relied on the multi-stacked photosensitive layers thus there remain challenges in spectral matching and interfaces contacting. Here, a structurally simple bidirectional and UV–vis dual-band OPD is proposed, with single photosensitive layer sitting between electrodes. By elaborately regulating the optical field distribution and vertical phase segregation of the bulk heterojunction (BHJ), this OPD presents completely distinct spectral response ranges under bidirectional illuminations. Finally, this OPD outputs outstanding self-powered UV and vis dual-band responsivities (up to 30 and 50 mA W^{-1}) as the light illuminates from forward and backward direction, respectively. In addition, a stable and reliable optical communication system is realized based on this OPD where the UV response conveys valid information and further superimposes vis response for encryption. This design concept offers a simple alternative for achieving varied response windows and opens up a novel optical encryption method, which has potential be applied in a close-range private communication process.

1. Introduction

Photodetectors are devices that convert optical signals into electrical signals, which can be divided into x-ray photodetectors, ultraviolet (UV) photodetectors, visible (Vis) light photodetectors, infrared (IR) photodetectors, and wide-band photodetectors covering multiple spectral bands according to the spectral response wavelengths.[1–5] Organic semiconductors with tunable optical bandgaps have been considered as promising candidates for specific spectral bands detection.[6–10] Apart from that, organic semiconductors have attractive properties including an easy-fabrication process, large-area production potential, and superior mechanical flexibility.[8,11–14]

The dual-band response in photodetector can generate distinguishable signals, including current signals with discrepancy of values or polarities under illumination of different wavelengths of light.[15–18] Inspired by chaos-based secure communications to hide the amplitude message in the encrypted signals of the transmitter,[19,20] we can establish a secure optical communication system with a dual-band photodetector. In this instance, the encrypted signals are based on the linear superposition of the UV light response signals and the Vis light response signals, which can overcome the limitation of the linear dynamic range in the single-band photodetector thus the valid information can be decoded accurately[21,22]

To realize specific spectral bands detection, several advances have been made in organic photodetectors (OPD) such as synthesizing organic semiconductors with novel chemical structures, regulating the thickness of bulk heterojunction (BHJ) for charge collection narrowing, and designing an optical micro cavity.[9,23–26] However, it remains a challenge in developing a photodetector with dual-band response. Previous solutions usually focused on the multi-stacked photosensitive layers (heterojunction stacking or single semiconductor stacking), dependent on the photosensitive layers with different spectral response band to realize dual-band response in a single photodetector,[27–31] further, most of them required assistant of bidirectional charge injection. Moreover, spectral matching and interfaces contacting in the multi-stacked structure complex the device fabrication process. Therefore, there is a difficulty to rationally design a photodetector with dual-band response through a simple device structure.

In our work, a bidirectional UV–vis dual-band OPD (structure, Ag/glass/ITO/P3HT:PC71BM (BHJ)/PH1000 with a single photosensitive layer is successfully developed.[32–34] We delicately design the BHJ thickness to regulate vertical phase

T. Yan, L. Su, L. Wu, X. Fang
Department of Materials Science
State Key Laboratory of Molecular Engineering of Polymers
Fudan University
Shanghai 200438, P. R. China
E-mail: lmw@fudan.edu.cn; xshfang@fudan.edu.cn
Z. Li, X. Fang
Institute of Optoelectronics
Fudan University
Shanghai 200433, P. R. China
L. Wu
College of Chemistry and Chemical Engineering
Inner Mongolia University
Hohhot 010021, P. R. China

**ADVANCED
SCIENCE NEWS**
www.advancedsciencenews.com

**ADVANCED
FUNCTIONAL
MATERIALS**
www.afm-journal.de

segregation of donors and acceptors in a proper degree, where the donor phases and the acceptor phases are enriched at the top or bottom surface, bringing about opportunities in realizing distinct spectral response range. Sliver (Ag) was further deposited on the substrate to narrow the forward response range to UV spectral range (<400 nm) by absorbing or reflecting visible light. As a result, self-powered responsivities to UV light are realized ($\approx$30 mA W^{-1}) while those to Vis light are highly suppressed as forward light illuminated. Meanwhile, self-powered responsivities to Vis light are realized ($\approx$50 mA W^{-1}) while these to UV light are suppressed as backward light illuminated. It is important to note that, based on this bidirectional and UV–vis dual-band response OPD, a communication system with two independent optical paths can be established, where one path of UV light is dedicated to convey the valid information and the other path of Vis light is dedicated to encrypt the valid information, guaranteeing a secure and reliable optical communication process.

2. Results and Discussion

OPD was fabricated with a structurally simple sandwich configuration ITO/BHJ film/PH1000 as shown in **Figure** 1a, where BHJ film was formed from the P3HT:PC71BM blended solution (Figure S1, Supporting Information). Excitons (electron-hole pairs) can be stimulated by the absorbed photons whether the light illuminated from the ITO side or PH1000 side and then separate into the free carriers driven by the force from P3HT / PC71BM interfaces without applied voltage. As a result, free electrons and holes will be collected under the effect of electric field from ITO and PH1000 electrodes, outputting self-powered photocurrents (Energy levels in Figure 1b

and Figure S2, Supporting information, are obtained from the references[14,35]).

In order to search for an optimum thickness of BHJ for dual-band response, OPDs with three different BHJ thicknesses of 140, 600, and 2000 nm are fabricated. Figure 1c,e,g and Figure 1d,f,h show responsivity curves of OPD when incident light illuminated from ITO side and PH1000 side, respectively. OPD with 140 nm BHJ has relatively broad response range from 300 nm to $\approx$650 nm and achieve its peak responsivity of $\approx$0.4 A W^{-1} as the light illuminated from both sides, despite there is a slight suppression in the wavelength from 400 to 500 nm as the light is illuminated from PH1000 side (Figure 1c,d). As the thickness of the BHJ increased to ultra-thick 2000 nm, both the band edge of response wavelengths red shift from $\approx$650 to $\approx$750 nm, with their self-powered responsivity peaks of $\approx$0.29 A W^{-1} at 600 nm and 0.06 A W^{-1} at 700 nm, as incident lights were illuminated from ITO and PH1000 side, respectively (Figure 1g,h).

In stark contrast to others, in OPD with 600 nm BHJ, the shapes of response curves are totally different under bidirectional illuminations. In this case, it depicts a broad-range of 300 to 650 nm wavelengths (peak responsivity of $\approx$0.4 A W^{-1}, Figure 1e) and a relative narrow-range of 500 to 700 nm (peak responsivity of $\approx$0.05 A W^{-1}, Figure 1f) wavelengths as was illuminated from ITO side and PH1000 side, respectively. This specific spectral range difference may become a good candidate for realizing an OPD with dual-band response. Its corresponding noise current and specific detectivities are shown in Figures S3 and S4 (Supporting Information).[36–38]

In order to deeply understand the reasons for the difference in spectral response curves, we begin with the definition of the responsivity, which represents the detective sensitivity of a photodetector, generally given by:[39,40]
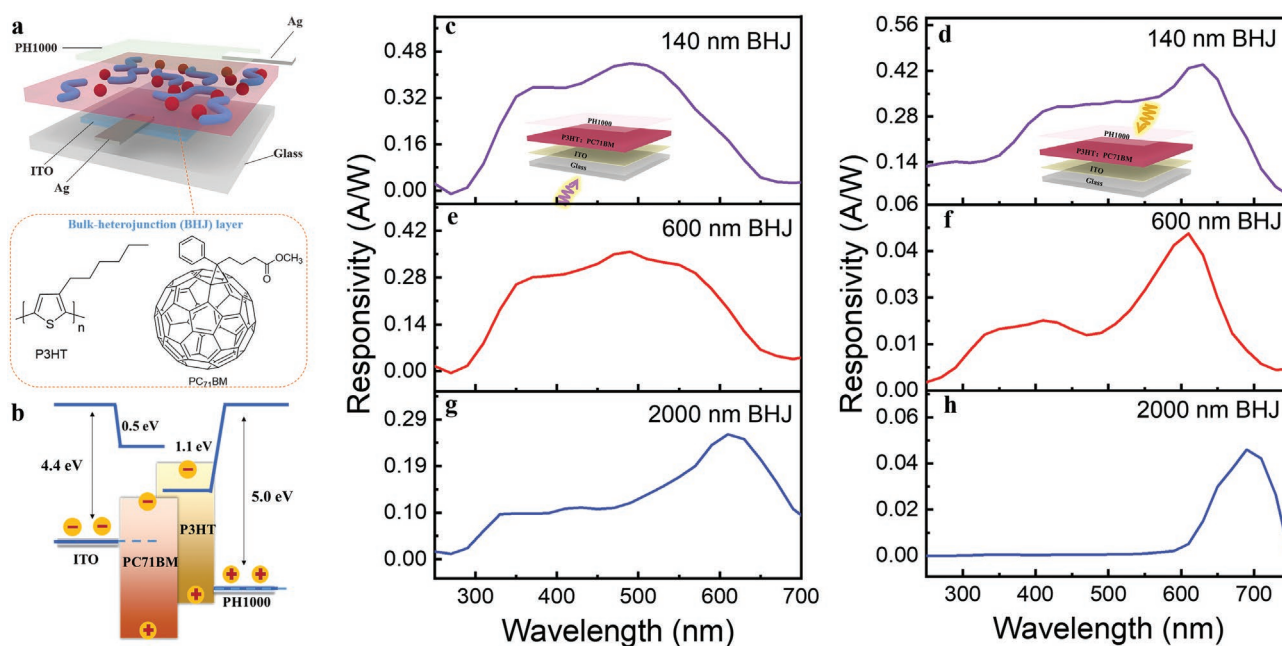

Figure 1. Device structure and spectral response range of OPD with varied BHJ thicknesses. a) Device structure. The bottom inset is the chemical structures of P3HT and PC71BM. b) Energy levels and carriers' migration in OPD (under illumination, at 0 V). Responsivities of OPD with varied BHJ thicknesses as incident light illuminated from c,e,g) ITO side and d,f,h) PH1000 side. The optoelectronic tests are conducted at 0 V.
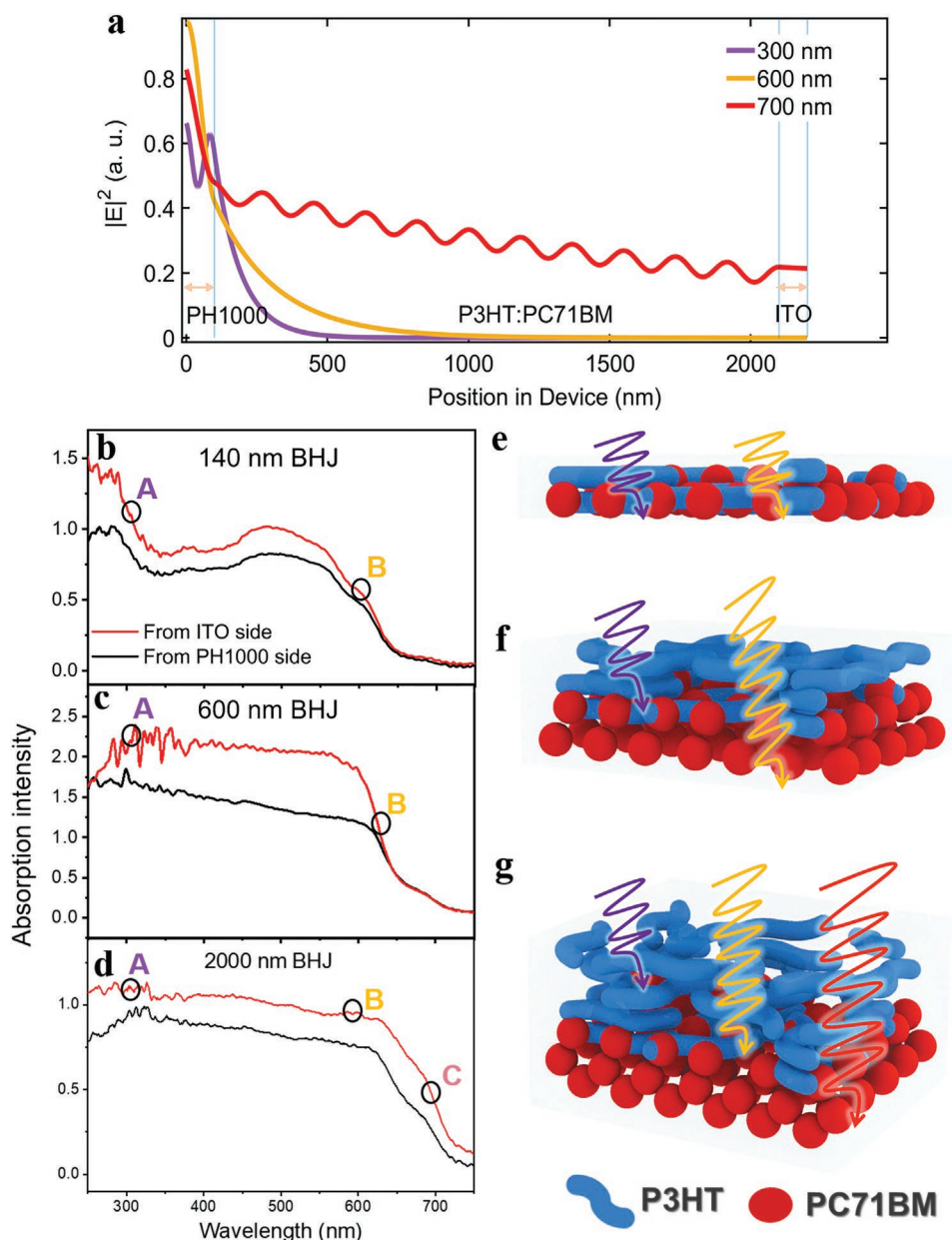
**ADVANCED
SCIENCE NEWS**

www.advancedsciencenews.com

**ADVANCED
FUNCTIONAL
MATERIALS**

www.afm-journal.de

Figure 2. Light absorption performance of BHJ with varied thicknesses. a) Optical field intensity distribution in OPD. Absorption intensity (red line: light incident from ITO side, black line: light incident from PH1000 side) of BHJ with varied thicknesses of b) 140 nm, c) 600 nm, and d) 2000 nm. Models of the light absorption performance (purple curve: 300 nm wavelength light, yellow curve: 600 nm wavelength light, red curve: 700 nm wavelength light) and distributions of P3HT phases and PC71BM phases of BHJ with varied thicknesses of e) 140 nm, f) 600 nm, and g) 2000 nm.

$$R_\lambda = \frac{I_{ph}}{PS} \tag{1}$$

where I_{ph} is the outputted photocurrent obtained under light illumination, P is the power density of the illumination light and S is the effective illumination area of the device. From the equation we can see I_{ph} is the key factor that is intensely in positive correlation of the R_λ, which is jointly dependent on the light absorption within the BHJ layer, the charge carrier generation quantum yield of the exciton and charge transfer state dissociation, and collection efficiency of the photo-generated charge carriers.[41] Beer-Lambert law reveals that the absorption

intensity of the material for a certain wavelength is exponentially dependent on its thickness, which is given by $I = I_0 e^{-\alpha x}$. Suppose that the charge generation quantum yield and photo-generated carriers' collection efficiency are fixed in OPDs with the same thickness of BHJ as the light illuminated either from ITO side or PH1000 side. A transfer matrix analysis is utilized to simulate the actual optical field distributions at different positions in OPDs to clarify its effect on spectral response discrepancy in OPDs with different thicknesses.[24]

Figure 2a simulates the optical field intensity of wavelength 300, 600, and 700 nm lights emitting across the OPD from PH1000 side, corresponding to the A, B and C region in the

**ADVANCED
SCIENCE NEWS**
www.advancedsciencenews.com

**ADVANCED
FUNCTIONAL
MATERIALS**
www.afm-journal.de

BHJ absorption intensity curves with different thicknesses (Figure 2b–d). Knowledge of the optical constants refractive indexes n and extinction coefficients k (see Figure S5, Supporting Information) helps to accurately build the actual optical field distribution. Wavelength 300 nm light is strongly absorbed within the position of 500 nm of the OPD (at 400 nm position of the BHJ) while the longer wavelength 600 nm light can reach the deeper position 1000 nm of the device (at 900 nm position of the BHJ). Contrary to others, wavelength 700 nm light can penetrate through the whole photosensitive layer although the thickness of BHJ is increased to 2000 nm, which can account for the red shift of the absorption edges in thick BHJ. Meanwhile, the absorption intensity obtained when the incident light illuminated from ITO side is higher than that from PH1000 side especially in 600 nm BHJ (Figure 2c), which is in consistence with the huge difference of peak responsivities in OPD with 600 nm BHJ (Figure 1e,f), which may arise from the vertical phase segregation of P3HT and PC71BM.[42]

Based on the above simulation of optical field, combined with the vertical phase segregation in P3HT:PC71BM system (will be discussed in the following part), models of light with different wavelengths transmitting in BHJ with varied thicknesses are schematically shown in Figure 2e–g. For the typical thin BHJ of 140 nm (Figure 2e), both wavelengths of ≈300 nm light and 600 nm light can penetrate the whole active layer, where P3HT phase and PC71BM phase are in a tiny phase segregation state in the direction perpendicular to the substrate, thus the OPD depicts broadband spectral response curves under illumination from ITO side and PH1000 side (Figure 1c,d). When BHJ thickness increases ≈600 nm (Figure 2f), marked vertical phase segregation occurs in P3HT:PC71BM blended film. PC71BM phases are enriched on the surface of the substrate glass/ITO and the P3HT phases are enriched in the upper surface of BHJ, while in the middle region P3HT phases and PC71BM phases are relatively uniformly blended. In this instance, photo-generated carriers can only be produced within the 400 nm depth of BHJ layer as ≈300 nm wavelengths illuminated, while photo-generated carriers can be produced in the entire photosensitive layer as stimulated by light with longer wavelengths ≈600 nm. This can account for the suppression of responsivity values in short-wavelength region in OPD with 600 nm BHJ (Figure 1f). When the BHJ thickness is further increased to 2000 nm (Figure 2g), light with wavelengths of ≈300 and 600 nm are constrained within thicknesses of ≈400 nm and 900 nm inside the photosensitive layer, which correspond to the P3HT-riched region and P3HT-riched/P3HT:PC71BM-blended region, respectively; thus the light responses of wavelengths shorter than 600 nm are strongly suppressed. However, light with wavelengths of ≈700 nm can penetrate through the entire photosensitive layer to produce photo-generated carriers, as a result depicting a narrow-band response ≈650 nm (Figure 1g,h).

We have discussed the influence of light absorption on the spectral response. It is demonstrated that OPDs with extremely thin (140 nm) and extremely thick (2000 nm) BHJ almost have similar spectral response shapes under bidirectional illuminations that basically depend on optical field intensity distribution in device. This is absolutely not the case in OPD with 600 nm BHJ, where the vertical phase separation of P3HT and PC71BM will have a profound impact on the completely different spectral response shapes. In other words, the ratio variation of P3HT and PC71BM in the upper and bottom surfaces of BHJ layer will intensely affect the excitons and charge transfer state dissociation, which will finally determine the photocurrents or responsivities of OPD. We then attempt to simulate the P3HT-rich and PC71BM-rich aggregation states of the upper and bottom surface layers in the 600 nm-thick BHJ by deliberately changing the component proportion of donor/acceptor in the 80 nm-thick BHJ and comparing their spectrum responsivity curves (light incident from the PH1000 side). This is based on two assumptions: there is nearly no vertical phase segregation within an 80 nm-thick BHJ layer; vertical phase segregation of the donor/acceptor phases dominates bidirectional shape difference of responsivity curves in OPD's with 600 nm thickness.

As shown in **Figure 3**a, OPDs ITO (100 nm) / BHJ (80 nm)/ PH1000 (100 nm) with ratios of P3HT:PC71BM of 7:3, 3:7, 1:9 are designed and their spectral response curves are given, respectively. As the ratio of P3HT:PC71BM is 1:9, the OPD demonstrates a wide response bandwidth from 300 to 650 nm. As the absolute amount of P3HT increases with the ratio of P3HT:PC71BM coming to 3:7, the OPD still has a relatively wide response band between 300 and 650 nm and the response peak appears ≈550 nm wavelengths. As the absolute amount of P3HT further increases with the ratio of P3HT:PC71BM coming to 7:3, the response band is narrowed to between 550 nm and 700 nm and its peak appears at ≈620 nm wavelengths. Compared the spectral response shapes of the OPDs here (Figure 3a) with those obtained in the OPD of 600 nm BHJ (Figure 1e,f), we can infer that the upper BHJ surface and the bottom BHJ surface corresponds to the P3HT-rich (P3HT:PC71BM ratio ≈7:3) and PC71BM-rich (P3HT:PC71BM ratio ≈1:9) region. Accordingly, we can further confirm that schematic diagrams in Figure 2e–g for understanding the working mechanisms of OPDs with varied BHJ thicknesses are scientific and realizable. Surface morphologies of BHJ are supported to clearly display the distribution of P3HT phase and PC71BM phase (Figure 3b–d), as the absolute amounts of P3HT increase, the second phase (P3HT) precipitates gradually on the surface and finally dominates (compared to the morphologies of pure PC71BM and P3HT in Figure 3e,f). Additional attention is paid to finely regulate the phase separation degree in P3HT:PC71BM by changing the annealing temperature to 0, 100 and 150 °C, but producing little effect (Figure S6, Supporting Information).

Consider now that we have obtained an OPD with 600 nm BHJ with forward broad-band UV to Vis and backward narrow-band Vis light responses from ITO side and PH1000 side, respectively. This distinct dual-response behavior on both sides provides a possibility for constructing a bidirectional UV–vis dual-band response device.

First, this OPD is an intrinsic narrow-band Vis photodetector as the light illuminates from PH1000 side. To this end, careful deposition of 50 nm-thick Ag layer was coated on the glass substrate to reflect or absorb the light with wavelengths >400 nm (**Figure 4**a), thus only 300–400 nm light can be utilized by OPD as it is illuminated from ITO side (Figure S7, Supporting Information). Consequently we obtain an UV/Vis dual-band response of 300–400 nm and 500–700 nm wavelengths (Figure 4c) under bidirectional illuminations. Figure 4b presents the current
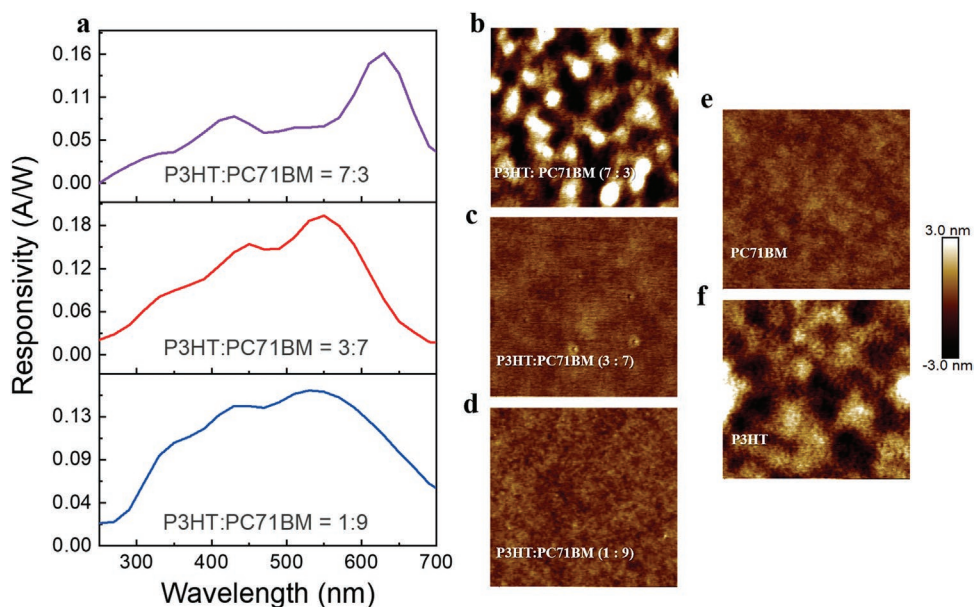
Figure 3. Spectral response ranges and morphologies of OPD with ultra-thin (80 nm) BHJ. a) Responsivities of OPD with varied P3HT and PC71BM ratios of P3HT:PC71BM=7:3 (purple line), P3HT:PC71BM=3:7 (red line), P3HT:PC71BM=1:9 (blue line). Surface morphologies (scale bar: 2 µm×2 µm) of BHJ film with b) P3HT:PC71BM=7:3, c) P3HT:PC71BM=3:7, d) P3HT:PC71BM=1:9, e) pure PC71BM film, f) pure P3HT film. The optoelectronic tests are conducted at 0 V.

density–voltage (*I–V*) curves of the OPD, showing rectifications effect when positive voltage is applied regardless of the illumination directions. Dark current density of the device is shown in Figure S8 (Supporting Information). Steady current–time (*I–t*) curves are conducted with 330 and 600 nm light on-off to demonstrate the outputed current signals in this device (Figure 4d). As the light is illuminated from ITO side, 330 nm

light can stimulate the device to output a high photocurrent of ≈5 µA, whereas 600 nm light can only stimulate the device to output an ultra-low photocurrent of ≈0.04 µA. By contrast, as the light is illuminated from PH1000 side, 330 nm light can only stimulate the device to output a ultra-low photocurrent of 0.08 µA, whereas 600 nm light can stimulate the device to output a high photocurrent of ≈10 µA. In addition, this OPD
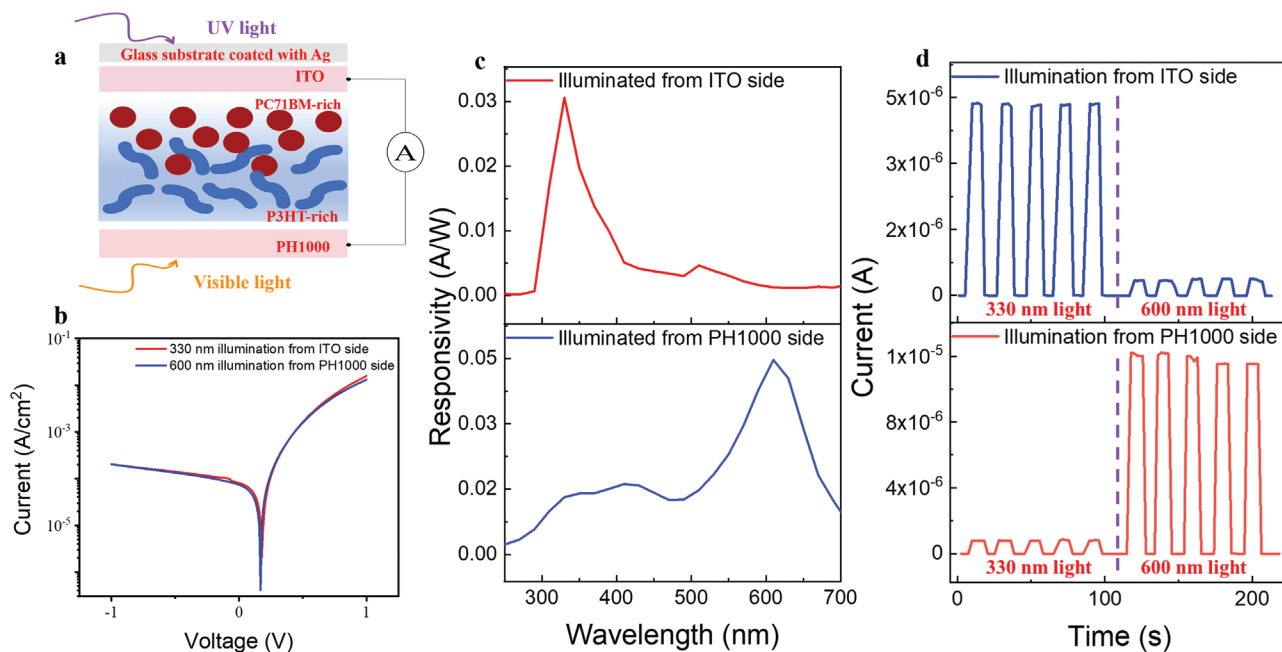

Figure 4. Optoelectronic performance of OPD with 600 nm BHJ. a) Device structure of OPD with dual-band response. b) Current-voltage curves. c) Responsivity curves, at 0 V. d) Current-Time curves, at 0 V, light power density 1.3 mW cm^{-2}.

presents a fast response of 0.7 ms to rise and 3.5 ms to decay at 0 V, as shown in Figure S9 (Supporting Information).

Traditional UV communication mode with single-band photodetector depicts terrible confidentiality due to the lack of straightforward and efficient encryption technique (Figure S10, Supporting Information).[43] In addition, encrypted UV communication can be realized by increasing the bits of digital signals with dual-band response to make it more difficult to crack the keys.[44] Further, our dual-band OPD can realize a double encryption for its distinct spectral response performance under bidirectional illuminations (Figure S11, Supporting Information). However, this encryption mode relies on increased digital bits and it will slow down optical communication process.

Thus, we proposed an optical encryption strategy to build a secure UV communication mode system based on our fabricated OPD with bidirectional dual-band response here (**Figure 5**a). See physical pictures of the bidirectional dual-band response OPD with dual light sources and schematic diagram of secure UV communication mode system shown in Figure S12 (Supporting Information). Forward UV responses (information signals) are used to convey the valid information, while the backward Vis light responses (coded signals) are used to encrypt the valid information to be the encrypted signals (information signals + coded signals) sent to the receiver. If the message is detected to be eavesdropped during this process, the optical communication process will be halted; if it is not eavesdropped, coded signals responding only to Vis light will be sent later, and thus the receiver can decrypt the encrypted signals and output the valid information signals (Figure 5b demonstrates the decoding process). This is an encrypted and secure UV communication mode, which can ensure that information is transmitted point-to-point from the sender to the receiver.

Figure 5c gives a living example to demonstrate the secure communication UV process. The green lines convey encrypted signals as UV light illuminated from forward direction and Vis light illuminated from backward direction simultaneously. The purple lines convey coding signals as only Vis light illuminated from backward direction. The blue lines convey unencrypted information signals as only UV light is illuminated from forward direction. The red lines convey decoded signals that are obtained by subtracting the purple coding signals from the green encrypted signals. As for the blue information
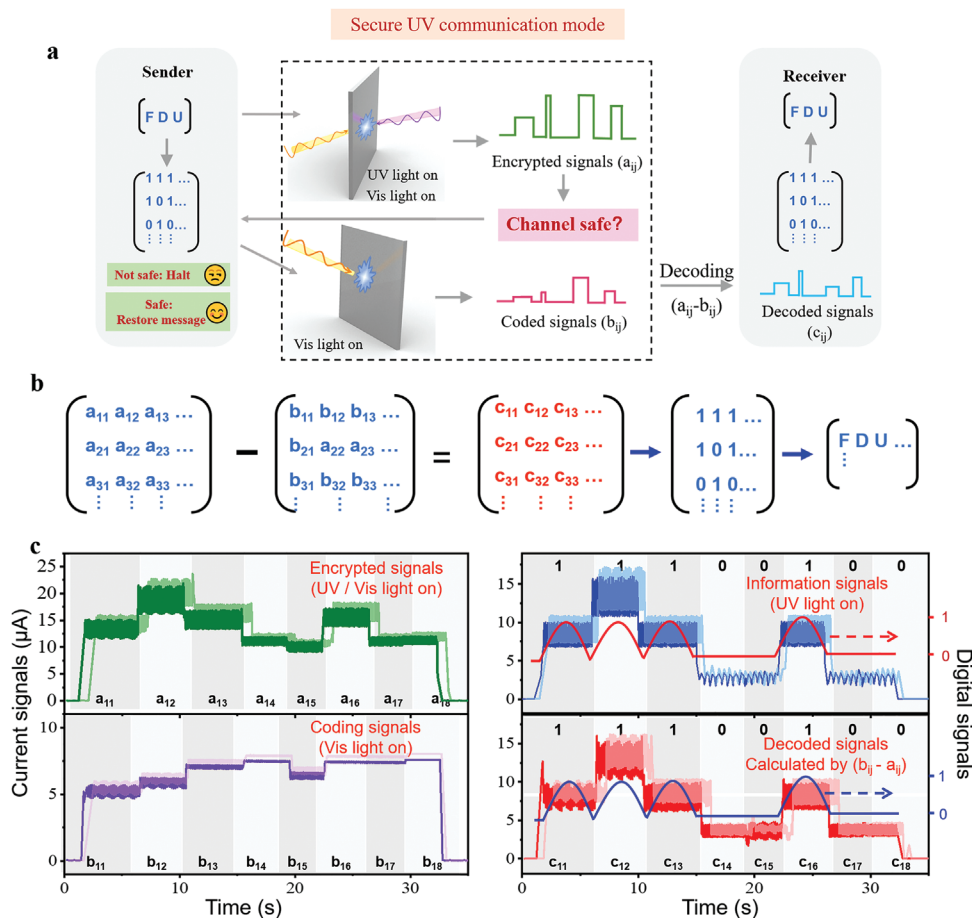

Figure 5. Demonstration of a secure optical communication system. a) Working principle of secure UV communication mode. b) Decoding formula of the optical communication system. c) A living example of an optical communication process, the green line is conducted as 310 and 660 nm simultaneously on, the blue line is conducted as only 310 nm UV light on, the purple light is conducted as only 660 nm light on, and the red light is obtained by subtract the purple signals from the green signals. The dark green, dark blue, dark purple, and dark red lines are performed in the dark environment. The light green, light blue, light purple and light red lines are performed under indoor environment illuminated by fluorescent lamp. All tests are performed at 0 V.

signals and red decoded signals, photocurrents >5 µA are defined as logical state 1 and <5 µA are defined as logical state 0 to facilitate information interaction with computers. It is found that the information signals can be well matched with the calculated decoded signals, indicating that the secure UV communication system is feasible in theory and in practice. In addition, the working results of the system under dark state (dark line) and under light state (light line) are measured, respectively (Figure 5c), and it is found that some ambient light will not affect the accuracy of UV communication process (Clearer results are shown in Figure S13, Supporting Information).

3. Conclusion

In summary, we introduce a simple device structure to fabricate a self-powered OPD with bidirectional UV–vis dual-band response by designing the optical field distribution and the vertical phase segregation of BHJ. The optimum BHJ of 600 nm thickness allows for obtaining a relatively narrow-band response toward Vis light (500–700 nm) by suppressing its optical field (of wavelengths <500 nm) at the deeper position. Moreover, vertical phase segregation of P3HT and PC71BM endows the distinct spectral response ranges as light irradiated in the opposite directions. This OPD demonstrates high self-powered photocurrents of 5 µA as 330 nm UV light illuminated from ITO side and 10 µA as 600 nm Vis light illuminated from PH1000 side. Hence, a secure UV communication system with two independent optical paths is realized based on our OPD, where one path expert for convey valid information and the other expert for encrypting the valid information, yielding a stable and reliable UV communication process. Beyond their superb performance in terms of its distinctive bidirectional UV–vis dual-band response and self-powered performance, further efforts are required to regulate its UV response to sun blind region (200–280 nm) for the realization of short-range anti-interference communication based on this structurally simple device.

4. Experimental Section

Materials: All solvents were purchased from Sinopharm China. Poly(3-hexylthiophene) (P3HT), Phenyl-C71-butyric-acid-methyl ester (PC71BM) were purchased from J&K Chemicals Inc. poly(3,4-ethylenedioxythiophene): poly(styrenesulfonate) (Clevios PH1000) with a solid content of 1.0–1.3% were purchased from Heraeus Inc., Germany. The Indium-doped tin oxide (ITO)-coated substrates were purchased from Youxuan, Liaoning Co., Ltd.

Device Fabrication: 20 mg P3HT and 30 mg PC71BM were dissolved in 0.5 mL chloroform and 0.5 mL 1,2-dichlorobenzene (o-DCB), and then stirred overnight at 55 °C to form a blended solution. Glasses with ITO substrates were ultrasonically cleaned with soapy water, deionized water, acetone and isopropanol for 20 min and plasma treatment for 5 min before use. The volume of PH1000 aqueous solution was diluted with ethanol to three times the original volume before used. P3HT:PC71BM solution was then spin-coated on substrates at 800 rpm min^{-1} and 200 rpm min^{-1} and baked at different temperatures for 10 min to form active layers of ≈600 and 2000 nm, respectively. To form an OPD with 140 nm BHJ, the P3HT and PC71BM blended solution was dilute to 25 mg ml^{-1} and spin-coated at a rate of 2000 rpm min^{-1}. To form OPDs with an ultra-thin BHJ (80 nm) of varied P3HT and PC71BM ratios, the blended solution was kept to be 25 mg ml^{-1} and spin-coated at a rate of 3000 rpm min^{-1}. PH1000 was then sprayed on a 120 °C hot plate and annealed at 120 °C for 20 min to form a 100 nm film. For the convenience of the optoelectronic measurements, the organic electrodes were extracted by silver paste. The PH1000 layer was fabricated in the air. The photosensitive layer P3HT:PC71BM was fabricated in the glove box with argon. All characterizations of the devices were conducted in the air condition. The effective illumination area of the device is defined by the overlapping area of upper and lower electrodes of ≈0.2 cm × 0.3 cm.

Device Characterization: The absorption intensities of photosensitive layers were calculated by ultraviolet-visible (UV–vis) spectrophotometer (Hitachi U-4100). The optoelectronic parameters (including photocurrent, current–voltage curves, on-off curves) of photodetectors were investigated by Keithley 4200 with the light source system consisting of a Xe lamp and a monochromator. LEDs with adjustable optical power of wavelengths of 310 and 660 nm were applied in the optical communication system. The power density was calibrated of optical power meter before use. Device's response time was conducted by a transient light response system with a neodymium-doped yttrium aluminum garnet (Nd:YAG) laser (Continuum Electro-Optics, MINILITE II, pulse duration: 3–5 ns, 355 nm). Noise current was measured by electronic noise test system (PDA, model: PX500). Surface morphologies were performed by atomic force microscope (AFM) (Bruker Multimode Catalyst). High-resolution image of photosensitive layer was conducted by TEM (JOEL JEM-2100F). The optical field distribution of OPD was simulated by optical admittance analysis and the wavelength-dependent, and refractive index (n) and extinction coefficients (k) of photosensitive layer were measured by the dual rotating-compensator Mueller matrix ellipsometer (ME-L ellipsometer, Wuhan Eoptics Technology Co.).

Supporting Information

Supporting Information is available from the Wiley Online Library or from the author.

Conflict of Interest

The authors declare no conflict of interest.

Data Availability Statement

The data that support the findings of this study are available in the supplementary material of this article.

**ADVANCED
SCIENCE NEWS**

www.advancedsciencenews.com

**ADVANCED
FUNCTIONAL
MATERIALS**

www.afm-journal.de

[1] Q. Li, J. van de Groep, Y. Wang, P. G. Kik, M. L. Brongersma, *Nat. Commun.* **2019**, *10*, 4982.

[2] S. Y. Li, Y. Zhang, W. Yang, H. Liu, X. S. Fang, *Adv. Mater.* **2020**, *32*, 1905443.

[3] Z. Q. Li, X. Liu, C. Zuo, W. Yang, X. S. Fang, *Adv. Mater.* **2021**, *33*, 2103010.

[4] M.-B. Lien, C.-H. Liu, I. Y. Chun, S. Ravishankar, H. Nien, M. Zhou, J. A. Fessler, Z. Zhong, T. B. Norris, *Nat. Photonics* **2020**, *14*, 143.

[5] Y. H. Chen, L. X. Su, M. M. Jiang, X. S. Fang, *J. Mater. Sci. Technol.* **2022**, *105*, 259.

[6] T. Yan, W. Song, J. Huang, R. Peng, L. Huang, Z. Ge, *Adv. Mater.* **2019**, *31*, 1902210.

[7] F.-H. Canek, W.-F. Chou, T. M. Khan, L. Diniz, J. Lukens, F. A. Larrain, V. A. Rodriguez-Toro, B. Kippelen, *Science* **2020**, *370*, .698

[8] J. H. Kim, A. Liess, M. Stolte, A. M. Krause, V. Stepanenko, C. Zhong, D. Bialas, F. Spano, F. Wurthner, *Adv. Mater.* **2021**, *33*, 2100582.

[9] A. Armin, R. D. Jansen-van Vuuren, N. Kopidakis, P. L. Burn, P. Meredith, *Nat. Commun.* **2015**, *6*, 6343.

[10] J. Huang, J. Lee, J. Vollbrecht, V. V. Brus, A. L. Dixon, D. X. Cao, Z. Zhu, Z. Du, H. Wang, K. Cho, G. C. Bazan, T. Q. Nguyen, *Adv. Mater.* **2020**, *32*, 1906027.

[11] H. Jinno, T. Yokota, M. Koizumi, W. Yukita, M. Saito, I. Osaka, K. Fukuda, T. Someya, *Nat. Commun.* **2021**, *12*, 2234.

[12] H. Lee, E. Kim, Y. Lee, H. Kim, J. Lee, M. Kim, o.-J. HYoo, S. Yoo, *Sci. Adv.* **2018**, *4*, eaas9530.

[13] S. Park, S. W. Heo, W. Lee, D. Inoue, Z. Jiang, K. Yu, H. Jinno, D. Hashizume, M. Sekino, T. Yokota, K. Fukuda, K. Tajima, T. Someya, *Nature* **2018**, *561*, 516.

[14] T. T. Yan, Z. Li, F. Cao, J. Chen, L. Wu, X. S. Fang, *Adv. Mater.* **2022**, *34*, 2201303.

[15] B. Ouyang, H. Zhao, Z. L. Wang, Y. Yang, *Nano Energy* **2020**, *68*, 104312.

[16] D. Wang, X. Liu, Y. Kang, X. Wang, Y. Wu, S. Fang, H. Yu, M. H. Memon, H. Zhang, W. Hu, Z. Mi, L. Fu, H. Sun, S. Long, *Nat. Electron.* **2021**, *4*, 645.

[17] W. Wang, M. Du, M. Zhang, J. Miao, Y. Fang, F. Zhang, *Adv. Opt. Mater.* **2018**, *6*, 1800249.

[18] X. Zhu, Y. Yan, L. Sun, Y. Ren, Y. Zhang, Y. Liu, X. Zhang, R. Li, H. Chen, J. Wu, F. Yang, W. Hu, *Adv. Mater.* **2022**, *34*, 2201364.

[19] M. Sciamanna, K. A. Shore, *Nat. Photonics* **2015**, *9*, 151.

[20] O. Spitz, A. Herdt, J. Wu, G. Maisons, M. Carras, C. W. Wong, W. Elsasser, F. Grillot, *Nat. Commun.* **2021**, *12*, 3327.

[21] C. Bao, Z. Chen, Y. Fang, H. Wei, Y. Deng, X. Xiao, L. Li, J. Huang, *Adv. Mater.* **2017**, *29*, 1703209.

[22] N. Wei, Y. Liu, H. Xie, F. Wei, S. Wang, L.-M. Peng, *Appl. Phys. Lett.* **2014**, *105*, 073107.

[23] K. H. An, B. O'Connor, K. P. Pipe, M. Shtein, *Org. Electron.* **2009**, *10*, 1152.

[24] Q. Lin, A. Armin, P. L. Burn, P. Meredith, *Nat. Photonics* **2015**, *9*, 687.

[25] L. Wang, Z. Li, M. Li, S. Li, Y. Lu, N. Qi, J. Zhang, C. Xie, C. Wu, L. B. Luo, *ACS Appl. Mater. Interfaces* **2020**, *12*, 21845.

[26] Y. Wang, J. Kublitski, S. Xing, F. Dollinger, D. Spoltore, J. Benduhn, K. Leo, *Mater Horiz* **2022**, *9*, 220.

[27] Z. Lan, Y. Lei, W. K. E. Chan, S. Chen, D. Luo, F. Zhu, *Sci. Adv.* **2020**, *6*, eaaw8065.

[28] Z. Lan, F. Zhu, *ACS Nano* **2021**, *15*, 13674.

[29] V. Pejović, E. Georgitzikis, I. Lieberman, P. E. Malinowski, P. Heremans, D. Cheyns, *Adv. Funct. Mater.* **2022**, *32*, 2201424.

[30] X. Tang, M. M. Ackerman, M. Chen, P. Guyot-Sionnest, *Nat. Photonics* **2019**, *13*, 277.

[31] B. Lan, X. Wu, F. Ma, L. Zhang, S. Yin, *ACS Appl. Mater. Interfaces* **2022**, *14*, 42277.

[32] J. E. Anthony, A. Facchetti, M. Heeney, S. R. Marder, X. Zhan, *Adv. Mater.* **2010**, *22*, 3876.

[33] A. Nawaz, M. S. Meruvia, D. L. Tarange, S. P. Gopinathan, A. Kumar, A. Kumar, H. Bhunia, A. J. Pal, I. A. Hümmelgen, *Org. Electron.* **2016**, *38*, 89.

[34] B. Xu, J. Hou, *Adv. Energy Mater.* **2018**, *8*, 1800022.

[35] L. C. Z. Xu, M. Chen, G. Li, Y. Yang, *Appl. Phys. Lett.* **2009**, *95*, 013301.

[36] F. Furlan, D. Nodari, E. Palladino, E. Angela, L. Mohan, J. Briscoe, M. J. Fuchter, T. J. Macdonald, G. Grancini, M. A. McLachlan, N. Gasparini, *Adv. Opt. Mater.* **2022**, *10*, 2201816.

[37] M. Kielar, O. Dhez, G. Pecastaings, A. Curutchet, L. Hirsch, *Sci. Rep.* **2016**, *6*, 39201.

[38] C. C. Lee, R. Estrada, Y. Z. Li, S. Biring, N. R. A. Amin, M. Z. Li, S. W. Liu, K. T. Wong, *Adv. Optical Mater.* **2020**, *8*, 2000519.

[39] Y. Fang, A. Armin, P. Meredith, J. Huang, *Nat. Photonics* **2018**, *13*, 1.

[40] F. Teng, K. Hu, W. Ouyang, X. S. Fang, *Adv. Mater.* **2018**, *30*, 1706262.

[41] D. M. N. M. Dissanayake, A. Ashraf, Y. Pang, M. D. Eisaman, *Adv. Energy Mater.* **2014**, *4*, 1300525.

[42] M. Campoy-Quiles, T. Ferenczi, T. Agostinelli, P. G. Etchegoin, Y. Kim, T. D. Anthopoulos, P. N. Stavrinou, D. D. Bradley, J. Nelson, *Nat. Mater.* **2008**, *7*, 158.

[43] H. Fang, C. Zheng, L. Wu, Y. Li, J. Cai, M. Hu, X. S. Fang, R. Ma, Q. Wang, H. Wang, *Adv Funct Mater* **2019**, *29*, 1809013.

[44] F. Cao, T. Yan, Z. Li, L. Wu, X. S. Fang, *Adv. Optical Mater.* **2022**, *10*, 2200786.